



Earth and Space Science

RESEARCH ARTICLE

10.1002/2014EA000089

Key Points:

- The horizontal wind model has been updated
- New data fill observational gaps
- Empirical specifications are consistent with ionospheric models

Supporting Information:

- Figures S1–S3
- Software S1

Correspondence to:

D. P. Drob,
douglas.drob@nrl.navy.mil

Citation:

Drob, D. P., et al. (2015), An update to the Horizontal Wind Model (HWM): The quiet time thermosphere, *Earth and Space Science*, 2, 301–319, doi:10.1002/2014EA000089.

Received 8 JAN 2015

Accepted 30 MAR 2015

Accepted article online 22 APR 2015

Published online 28 JUL 2015

An update to the Horizontal Wind Model (HWM): The quiet time thermosphere

**Douglas P. Drob¹, John T. Emmert¹, John W. Meriwether², Jonathan J. Makela³, Eelco Doornbos⁴,
Mark Conde⁵, Gonzalo Hernandez^{6,7}, John Noto⁸, Katherine A. Zawdie¹, Sarah E. McDonald¹,
Joe D. Huba⁹, and Jeff H. Klenzing¹⁰**

¹Space Science Division, Naval Research Laboratory, Washington, District of Columbia, USA, ²Department of Physics and Astronomy, Clemson University, Clemson, South Carolina, USA, ³Department of Electrical and Computer Engineering, University of Illinois at Urbana-Champaign, Urbana, Illinois, USA, ⁴Department of Earth Observation and Space Systems, Technical University Delft, Delft, Netherlands, ⁵Geophysical Institute, University of Alaska Fairbanks, Fairbanks, Alaska, USA, ⁶Department of Earth and Space Sciences, University of Washington, Seattle, Washington, USA, ⁷Deceased 15 July 2014, ⁸Scientific Solutions Inc., Chelmsford, Massachusetts, USA, ⁹Plasma Physics Division, Naval Research Laboratory, Washington, District of Columbia, USA, ¹⁰Space Weather Laboratory, Goddard Spaceflight Center, Greenbelt, Maryland, USA

Abstract The Horizontal Wind Model (HWM) has been updated in the thermosphere with new observations and formulation changes. These new data are ground-based 630 nm Fabry-Perot Interferometer (FPI) measurements in the equatorial and polar regions, as well as cross-track winds from the Gravity Field and Steady State Ocean Circulation Explorer (GOCE) satellite. The GOCE wind observations provide valuable wind data in the twilight regions. The ground-based FPI measurements fill latitudinal data gaps in the prior observational database. Construction of this reference model also provides the opportunity to compare these new measurements. The resulting update (HWM14) provides an improved time-dependent, observationally based, global empirical specification of the upper atmospheric general circulation patterns and migrating tides. In basic agreement with existing accepted theoretical knowledge of the thermosphere general circulation, additional calculations indicate that the empirical wind specifications are self-consistent with climatological ionosphere plasma distribution and electric field patterns.

1. Introduction

The basic behavior of the low-latitude and midlatitude thermosphere winds was first successfully modeled by Geisler [1967] and Kohl and King [1967]. The circulation is predominantly driven by the tidal pressure gradients caused by in situ EUV absorption that results in day-to-night temperature differences of ~ 200 K during solar minimum and ~ 350 K during solar maximum conditions [Jacchia, 1965; Hedin, 1987]. Early satellite observation by the National Aeronautics and Space Administration (NASA) Atmosphere Explorer (AE) satellite [Hedin et al., 1988], along with ground-based 630 nm Fabry-Perot Interferometer (FPI) measurements [Hernandez and Roble, 1976; Sipler et al., 1982; Burnside and Tepley, 1989], and Incoherent Scatter Radar (ISR)-derived thermospheric winds [Salah and Holt, 1974; Buonsanto et al., 1989] validate this early basic understanding. Beside the dominant role of photochemical production and loss, thermosphere neutral winds (specifically the general circulation and migrating tides) are one of the primary drivers of the time-dependent global morphology of the ionosphere.

At high-latitudes, perturbations to the global solar pressure gradient wind patterns are driven by auroral and joule heating, as well as ion-neutral coupling to the high-latitude ion convection pattern [Killeen et al., 1982; Roble et al., 1983]. Early ground-based 630 nm FPI measurements [Hays et al., 1979], along with satellite observation by the NASA Dynamics Explorer satellite (DE2) [Spencer et al., 1981; Hays et al., 1981], lead to this understanding. The fundamental physics and morphology of these processes are mostly understood. The main characteristics can be simulated from first principles with thermosphere general circulation models such as the thermosphere ionosphere electrodynamics general circulation model (TIEGCM) [Richmond et al., 1992], the coupled thermosphere-ionosphere model [Fuller-Rowell and Rees, 1980], and the global ionosphere thermosphere model [Ridley et al., 2006].

While the predominant behavior of the thermospheric general circulation is understood [Rishbeth, 1972; Killeen, 1987], meteorological aspects of the momentum budget resulting from wave-wave interactions,

©2015. The Authors.

This is an open access article under the terms of the Creative Commons Attribution-NonCommercial-NoDerivs License, which permits use and distribution in any medium, provided the original work is properly cited, the use is non-commercial and no modifications or adaptations are made.

dynamical forcing from below, and ion-neutral coupling are not. This is despite the fact that significant day-to-day variability has long been observed in ground-based FPI wind measurements. Only with new coupled lower, middle, and upper atmosphere models [e.g., Roble, 2000] are these aspects now beginning to be resolved. These new coupled atmospheric models include fully free-running whole-atmospheric models [Liu et al., 2010; Jin et al., 2011; Akmaev, 2011], as well as coupled hybrid models that use outputs from assimilative numerical weather prediction systems [Siskind and Drob, 2014]. Meteorological forcing are either specified as time-dependent lower boundary conditions [Mendillo et al., 2002; Siskind et al., 2012] or via nudging techniques [Sassi et al., 2013; Siskind et al., 2014]. It is now well accepted that wave coupling from below is a major source of the observed day-to-day variability of the ionosphere [Fang et al., 2013].

With the ever increasing complexity of thermosphere-ionosphere models, it is equally important to have reliable observationally derived climatological specifications of the neutral wind fields to validate physical understanding and to serve as a benchmark for new observations. The Horizontal Wind Model (HWM) [Hedin et al., 1988, 1991; Drob et al., 2008; Emmert et al., 2008] is the most comprehensive empirical specification available. The empirical model describes the atmosphere's vector wind fields from the surface to the exobase (~450 km) as a function of latitude, longitude, altitude, day of year, and time of day. HWM accounts for the annual and semiannual variations of the zonal mean general patterns, recurring global-scale stationary planetary waves, and the migrating diurnal, semidiurnal, and terdiurnal tides. The empirical formulation is able to represent the predominant variations of middle and upper atmosphere to an acceptable degree, because unlike the quasi-random weather in troposphere, these oscillations are periodic, driven by in situ solar heating under the cyclical influence of the Earth's rotation, tilt, and orbit around the Sun.

Where appropriate, HWM reduces the computational complexity of theoretical and applied calculations by avoiding the need to simultaneously compute the wind fields from first principles. For example, HWM provides realistic observational based drivers of the neutral winds for ionospheric model development and space weather applications [e.g., Huba et al., 2009; Kelly et al., 2014]. As mentioned, HWM also provides a convenient and reliable reference for the validation and tuning of general circulation models. HWM also provides a reasonable first guess, as well as a priori boundary conditions, for in situ and remote sensing data retrieval algorithms [e.g., Drob et al., 2009; Doornbos et al., 2010].

This paper describes recent upgrades to the quiet time component of the horizontal wind model (HWM) to address shortcomings of the previous version identified by new observation, as well as theoretical considerations. The recent observations include those of Meriwether et al. [2011] and Makela et al. [2013] who found disagreement with the HWM07 equatorial nighttime zonal winds. In tandem, first-principles ionospheric calculations using the HWM07 over the earlier HWM93 produced unsatisfactory results for some times and locations. For example, Huba et al. [2010] reported difficulties in predicting the observed morphology and drift rate of Equatorial Spread F bubbles for spring equinox conditions with HWM07, but not with HWM93. Improvements to HWM14 are primarily in the upper thermosphere (above 120 km) with only lesser changes at lower altitudes. In addition the geomagnetic storm time component of HWM, DWM07 [Emmert et al., 2008] is unchanged. The new HWM14 end user FORTRAN-90 subroutines and coefficient files are available in the online supporting information of this article.

This paper is organized as follows. Section 2 describes the HWM model formulation, parameter estimation procedure, and new data sets. Section 3 presents data-model and model-model comparisons to highlight the main results of this update. It describes statistical performance measures, the thermospheric zonal mean circulation, equatorial local time variations, and the quiet time high-latitude winds. Section 4 discusses self-consistency of the wind fields with modeled ionospheric structure, known limitations of the present model, and the way forward to future improvements.

2. Methodology

As an empirical model, HWM provides a readily accessible statistical view of a comprehensive observational database. In this approach the salient features of the data are identified and an appropriate mathematical basis set that can represent the features chosen. The unknown model parameters (together with the resolution of the basis functions to avoid underfitting and overfitting of the available data) are determined via an optimal estimation procedure. The resulting model is assumed to be valid within the chosen model ansatze, resolution, and observational uncertainty. The resulting model uncertainties are of two types; the natural variability of the system that cannot be (or is not) represented by the chosen model basis and the

Table 1. New Data Sets Added to the Prior Observational Database Described in *Drob et al. [2008]*

Instrument	Location	Height (km)	Years	Local Time	Days	Points	Reference
<i>Fabry-Perot Interferometer</i>							
Arecibo	18.7°N, 67.5°W	250	2012–2013	nighttime	428	29,434	<i>Ruan et al. [2013]</i>
Arequipa	16.47°S, 71.49°W	250	2007–2013	nighttime	260	16,447	<i>Meriwether et al. [2008]</i>
Jicamarca	11.96°S, 76.86°W	250	2009–2013	nighttime	318	10,056	<i>Meriwether et al. [2008]</i>
Movil	14.97°S, 74.89°W	250	2011–2013	nighttime	293	10,412	<i>Meriwether et al. [2008]</i>
PARI ^a	35.2°N, 82.85°W	250	2011–2013	nighttime	166	12,610	<i>Makela et al. [2012]</i>
Poker Flat ^b	65.1°N, 147.5°W	250	2009–2011	nighttime	297	5,983,090	<i>Conde and Smith [1995]</i>
RENOIR ^c	6.89°S, 38.56°W	250	2009–2012	nighttime	637	37,301	<i>Makela et al. [2013]</i>
South Pole	90.0°S	250	1989–1999	nighttime	1,091	198,560	<i>Hernandez et al. [1992]</i>
<i>Satellite</i>							
GOCE ^d	± 83.4°	253–295	2009–2012	twilight	813	6,613,172	<i>Doornbos et al. [2010]</i>

^aPisgah Astronomical Research Institute.^bImaging FPI.^cRelocatable Equatorial Nighttime Observatory of Ionospheric Regions.^dCross track only.

observational uncertainties of the individual measurements. This approach follows the earliest forms of operational numerical weather prediction data assimilation techniques known as function fitting [Daley, 1993]. Unlike for tropospheric meteorology, the observed first-order time evolution of the system is periodic in nature over both diurnal and annual time scales because the upper atmospheric general circulation is predominantly an externally driven system.

2.1. New Data/Observational Database

An important aspect of HWM model coefficient estimation is the analysis and comparison of overlapping, partially overlapping, and disparate data sets. Data-data and model-data comparisons facilitate identification of outlying data sets, as well as validation of new instruments and measurement techniques. The previous HWM database described by *Drob et al. [2008, and references therein]* includes over 60×10^6 observations from 35 different instruments spanning over 50 years. These historical data are available from both ground- and space-based techniques. The ground-based techniques include optical 630 nm FPI measurements and ISR measurements. The satellite techniques include optical techniques and in situ mass spectrometer measurements. Table 1 shows a summary of the new upper thermospheric observations added to the database. The new data set includes $\sim 13 \times 10^6$ observations made over the last 10 years from six new instruments and two existing instruments. The update also includes the South Pole FPI measurements from 1989 to 1999 which were excluded from HWM07 fits. Overall, the HWM14 is a synthesis of $\sim 73 \times 10^6$ measurements from 44 different instruments spanning over 60 years. For reasons described below, HWM14 excludes the nighttime 630 nm Upper Atmospheric Research Satellite (UARS), Wind Imaging Interferometer (WINDII) measurements that were included in HWM07. It is noted here that while the new data improves the spatiotemporal coverage of the HWM database (see, for example, Figure 1 of *Drob et al. [2008]*), the entire database is biased low with respect to solar cycle coverage. The details and implications of this are described later.

The majority of new data is from ground-based measurement of the 630 nm OI nightglow feature that has a peak volume emission at an altitude of ~ 250 km and a half width of ~ 60 km. Traditionally, the horizontal wind vector is determined from four cardinal line-of-sight Doppler velocities along with a vertical zero-wind reference measurement. New data include multi-instrument common volume observations providing improved measures of the horizontal and vertical wind vector, as well as regional spatial gradients [Makela et al., 2012, 2013]. Additionally, Scanning Doppler Interferometer FPI measurements from *Conde and Smith [1995, 1998]* provide dense maps of the local thermospheric wind field at high latitude.

The second type of data that contributed to the HWM upgrade is the cross-track winds from the European Space Agency, Gravity Field and Steady State Ocean Circulation Explorer (GOCE) satellite. GOCE operated in a near-circular Sun-synchronous terminator orbit from March 2009 to November 2013. GOCE cross-track wind measurements are predominantly zonal because of the satellite's 96.7° inclination. GOCE provides important measurements at dawn and dusk local times that are historically difficult to measure by

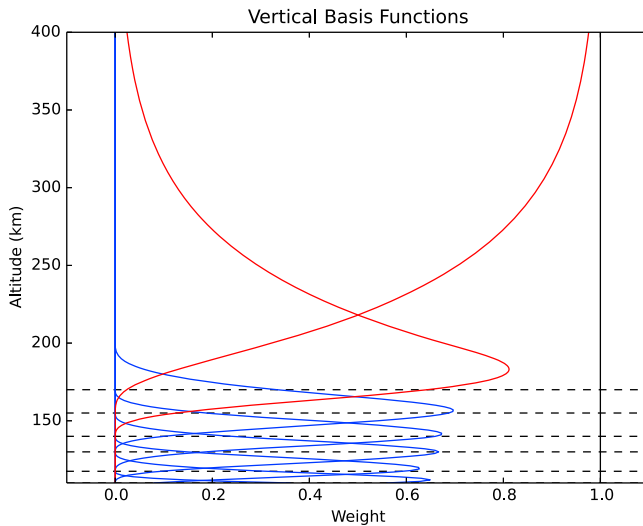


Figure 1. Vertical cubic B-spline basis functions β_j (red, blue) and corresponding data intervals δ_j (dashed) for the new HWM model. The last two basis functions (red) are constructed to approach either 0 or 1, subject to continuity and derivative constraints with the remaining functions.

space- and ground-based optical techniques. Details from the GOCE cross-track wind measurement technique are provided by *Doornbos et al.* [2010, 2014].

Other available observations not yet in the HWM database are magnetic meridional winds derived from ionosonde measurements [Richards, 1991], cross-track wind derived from high-precision acceleration measurements made by the CHAllenging Minisatellite Payload (CHAMP) satellite [Liu et al., 2006; Lühr et al., 2007], and space-based FPI measurements of the lower thermosphere from the NASA Thermosphere, Ionosphere, Energetics and Dynamics mission (TIMED) Imaging Doppler Interferometer (TIDI) [Killeen et al., 2006]. These data sets were not included in order to focus on the new ground-based data sets where discrepancies in HWM07 were identified. In the future the omitted data sets can provide independent validation, as well as be used to improve HWM, in particular, to resolve and account for the solar flux dependence of thermospheric winds.

2.2. Model Formulation

The quiet time component of HWM provides average horizontal winds as a function of day of year τ , solar local time δ , colatitude θ , longitude ϕ , and altitude z from the ground to the exobase. The atmosphere's dominant recurring cyclical climatological variations are represented by height-modulated vector spherical harmonic basis functions:

$$U(\tau, \delta, \theta, \phi, z) = \sum_j \beta_j(z) u_j(\tau, \delta, \theta, \phi), \quad (1)$$

where $\beta_j(z)$ is the amplitude of the j th vertical cubic B-spline weighting kernel (shown in Figure 1) and $u_j(\tau, \delta, \theta, \phi)$ represents the periodic horizontal spatiotemporal variations for the j th vertical kernel. In this case $U(\tau, \delta, \theta, \phi, z)$ represents the zonal wind. The relation for the meridional wind component is given later. Each altitude interval contains four non-zero kernels ($j, j+1, j+2, j+3$) with the exception of the last altitude interval. Above 117.5 km the spacing of the intervals has been slightly revised from HWM07 to reduce the ringing of the second to the last kernel.

The horizontal variations $u_j(\tau, \delta, \theta, \phi)$ for the j th vertical model kernel are given by

$$\begin{aligned} u_j(\tau, \delta, \theta, \phi) &= \sum_{s=0}^S \sum_{n=1}^N \Psi_j^1(\tau, \theta, s, n) \\ &+ \sum_{s=0}^S \sum_{l=1}^L \sum_{n=l}^N \Psi_j^2(\tau, \delta, \theta, s, l, n) \\ &+ \sum_{s=0}^S \sum_{m=1}^M \sum_{n=m}^N \Psi_j^3(\tau, \phi, \theta, s, m, n). \end{aligned} \quad (2)$$

Table 2. Statistical Measures of Biases μ_q and Root-Mean-Square Error σ_q^{rms} for Various Models and Data Groups^a

Instrument	Points	μ_{obs}	μ_{93}	μ_{07}	μ_{14}	σ_{obs}	σ_{93}^{rms}	σ_{07}^{rms}	σ_{14}^{rms}
<i>Line of Sight, Fabry-Perot Interferometer (FPI), and Incoherent Scatter Radar (ISR)</i>									
Arecibo (ISR)	8051	11.62	-2.59	-9.25	-5.58	34.09	33.97	35.54	30.84
Arrival Height (FPI)	138690	-14.56	-13.19	-0.59	-6.74	103.55	101.06	68.60	69.07
Millstone Hill (ISR)	7503	-20.05	-9.76	-12.50	-9.92	59.95	48.42	47.71	45.79
Resolute Bay (FPI)	17377	0.41	-0.83	2.17	0.52	107.91	65.74	71.30	67.98
Søndrestrøme (ISR)	3730	2.97	-15.97	-27.72	-8.82	110.57	87.24	93.62	81.23
<i>Cross Track, Satellite</i>									
AE-E NATE	57428	7.74	7.76	5.31	1.81	68.73	56.58	55.40	51.40
GOCE	573672	95.79	19.58	40.46	6.81	48.83	50.41	60.60	36.05
<i>Meridional, Fabry-Perot Interferometer</i>									
Arecibo	81552	-12.05	3.97	-0.03	3.32	39.46	37.72	36.88	35.38
Arequipa	108139	1.80	4.11	3.57	-1.21	69.92	66.61	66.37	65.14
Halley Bay	91205	25.35	-19.62	12.59	0.68	88.48	72.50	68.87	63.51
Jicamarca	2054	-1.95	5.62	-1.68	2.02	42.42	41.60	40.96	39.11
Millstone Hill	68185	-46.01	-6.70	-20.80	-2.28	76.85	66.72	71.69	66.17
Mount John	1949	48.15	7.77	45.93	16.31	55.84	47.41	67.39	46.07
Movil	37725	0.33	0.54	-2.87	-3.54	47.32	44.78	46.80	44.98
PARI	21306	-28.56	18.24	-3.83	7.60	53.17	52.94	50.34	48.66
Poker Flat	450914	-22.51	69.54	6.72	0.22	54.29	100.46	59.99	47.65
RENOIR	12690	2.49	-1.19	-2.30	-2.91	45.40	36.46	43.13	36.10
Søndrestrøme	10303	-67.35	-0.77	-10.17	-8.81	103.26	90.50	82.58	86.97
South Pole	198560	2.94	-1.20	8.59	2.84	93.89	86.88	78.50	70.63
Svalbard	1381	-32.60	30.70	-0.58	-7.90	124.67	110.60	101.06	102.42
Thule	15519	-13.55	-6.17	12.89	8.66	127.32	107.24	93.42	93.92
Watson Lake	4890	-33.10	31.29	-1.30	-5.20	68.28	88.40	60.92	58.98
<i>Meridional, Satellite/Rocket</i>									
DE2 FPI 630 nm	6000	28.21	-4.68	2.45	2.78	108.31	78.94	77.45	81.64
TMA	2772	-7.13	-10.55	3.26	-1.60	69.70	72.68	43.55	46.45
UARS WINDII 557.7 nm	413449	2.50	-2.90	-0.04	-0.02	65.98	60.31	52.89	52.50
<i>Zonal, Fabry-Perot Interferometer</i>									
Arecibo	79108	36.77	12.65	-8.04	-6.19	52.66	53.07	47.59	44.71
Arequipa	99198	84.48	-25.81	-3.84	0.74	71.66	78.52	72.13	68.83
Halley Bay	91245	14.85	15.51	-5.13	-9.07	93.81	93.29	66.44	65.35
Jicamarca	1901	48.33	-43.89	-23.19	-7.74	59.29	79.79	64.31	59.54
Millstone Hill	68175	22.12	28.37	-9.74	-9.62	70.32	68.29	63.56	63.21
Mount John	1949	35.17	-1.38	-8.55	1.70	70.81	49.92	56.79	54.97
Movil	24227	63.54	-26.99	-9.16	4.39	55.55	60.72	56.49	48.35
PARI	12610	35.01	15.84	-27.40	-13.64	57.67	51.25	56.36	51.32
Poker Flat	450925	-14.35	-4.16	0.49	-9.09	70.35	65.00	72.56	60.30
RENOIR	12483	57.23	-34.74	-6.05	-0.71	44.94	63.27	46.09	40.32
Søndrestrøme	10442	-15.31	20.62	-7.31	-3.94	102.68	114.75	97.96	104.09
Svalbard	1353	-40.74	8.83	-3.57	-9.32	129.08	140.66	125.08	129.76
Thule	15643	2.78	27.58	-1.95	-7.45	150.12	133.50	118.98	118.30
Watson Lake	4979	-20.23	52.09	13.47	5.69	67.85	86.19	68.89	64.96
<i>Zonal, Satellite, and Rocket</i>									
DE2 WATS	7233	-19.95	1.00	-6.92	-6.52	125.73	88.99	89.17	94.83
TMA Release	2774	9.40	-2.02	6.37	-5.82	53.60	57.35	34.79	33.21
UARS WINDII 557.7 nm	415238	-39.77	-8.32	-4.37	-5.19	72.22	72.03	59.50	59.31

^aThe best and worst scores are highlighted in bold and italics, respectively.

Equation (2) includes the annual and semiannual harmonics $\Psi_j^1(\tau, \theta, s, n)$ for the zonal mean general circulation expressed in terms of the seasonal wave number s up to $S = 2$; the westward migrating diurnal, semidiurnal, and terdiurnal harmonics $\Psi_j^2(\tau, \delta, \theta, s, l, n)$ expressed in tidal wave number l up to $L = 3$; and the stationary planetary wave harmonics $\Psi_j^3(\tau, \phi, \theta, s, m, n)$ with longitudinal wave number m up to $M = 2$. Both the tidal and stationary planetary wave harmonics also include annual and semiannual amplitude modulation terms ($s = 1, s = 2$). The maximum order in latitude for all three sums is $N = 8$.

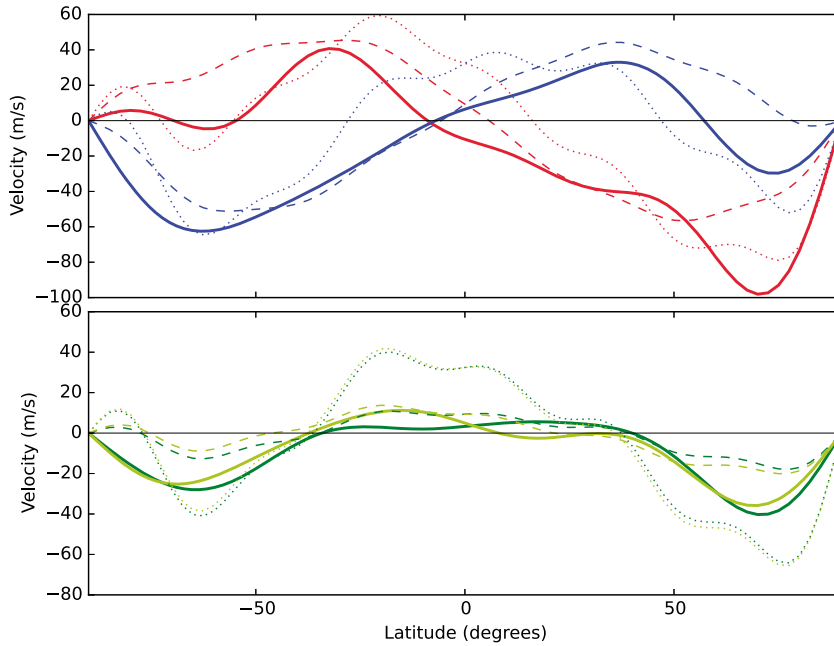


Figure 2. The zonally averaged zonal wind at 300 km during December solstice (blue), June solstice (red), March equinox (green), and September equinox (yellow green) from HWM14 (solid). Results from HWM93 are shown for the solar flux conditions of $F_{10.7} = 90$ (dashed) and $F_{10.7} = 180$ (dotted).

Unlike HWM07, in which the zonal mean variations Ψ_j^1 are expressed as a full vector spherical harmonic basis, the HWM14 formulation has been revised to ensure that the zonally averaged zonal and meridional winds are always zero exactly at the poles. The revised HWM zonal mean basis functions Ψ_j^1 are

$$\begin{aligned}\Psi_j^1(\tau, \theta, s, n) = & -C_{r,j}^{s,n} \cdot \sin(n\theta) \cdot \cos(s\tau) \\ & + C_{i,j}^{s,n} \cdot \sin(n\theta) \cdot \sin(s\tau),\end{aligned}\quad (3)$$

where $\{C_{r,j}^{s,n}, C_{i,j}^{s,n}\}$ are unknown model parameters $\mathbf{m}_j^{(1)}$ estimated from the observational database \mathbf{d} .

As in HWM07 the basis functions for the westward migrating tidal components are expressed in terms of Fourier-modulated vector spherical harmonics:

$$\begin{aligned}\Psi_j^2(s, l, n, \tau, \delta, \theta) = & -C_{a,r,j}^{s,l,n} \cdot V_n^l(\theta) \cdot \cos(l\delta) \cdot \cos(s\tau) \\ & + C_{a,i,j}^{s,l,n} \cdot V_n^l(\theta) \cdot \sin(l\delta) \cdot \cos(s\tau) \\ & - B_{a,r,j}^{s,l,n} \cdot W_n^l(\theta) \cdot \cos(l\delta) \cdot \cos(s\tau) \\ & - B_{a,i,j}^{s,l,n} \cdot W_n^l(\theta) \cdot \sin(l\delta) \cdot \cos(s\tau) \\ & - C_{b,r,j}^{s,l,n} \cdot V_n^l(\theta) \cdot \cos(l\delta) \cdot \sin(s\tau) \\ & + C_{b,i,j}^{s,l,n} \cdot V_n^l(\theta) \cdot \sin(l\delta) \cdot \sin(s\tau) \\ & - B_{b,r,j}^{s,l,n} \cdot W_n^l(\theta) \cdot \cos(l\delta) \cdot \sin(s\tau) \\ & - B_{b,i,j}^{s,l,n} \cdot W_n^l(\theta) \cdot \sin(l\delta) \cdot \sin(s\tau),\end{aligned}\quad (4)$$

where $\{C_{a,r,j}^{s,l,n}, \dots, B_{b,i,j}^{s,l,n}\}$ are the unknown vector spherical harmonic coefficients $\mathbf{m}_j^{(2)}$, estimated from the available observational data sets \mathbf{d} . Similarly, the stationary planetary wave harmonics $\Psi_j^3(\tau, \phi, \theta, s, m, n)$ are given by equation (4) replacing l with m and δ with ϕ , where their unknown model coefficients are $\mathbf{m}_j^{(3)}$.

The vector spherical harmonic basis functions $V_n^l(\theta), W_n^l(\theta)$ are related to the scalar normalized associated Legendre polynomials $P_n^l(\theta)$ by

$$V_n^l(\theta) = \frac{1}{\sqrt{n(n+1)}} \frac{d}{d\theta} P_n^l(\theta) \quad (5)$$

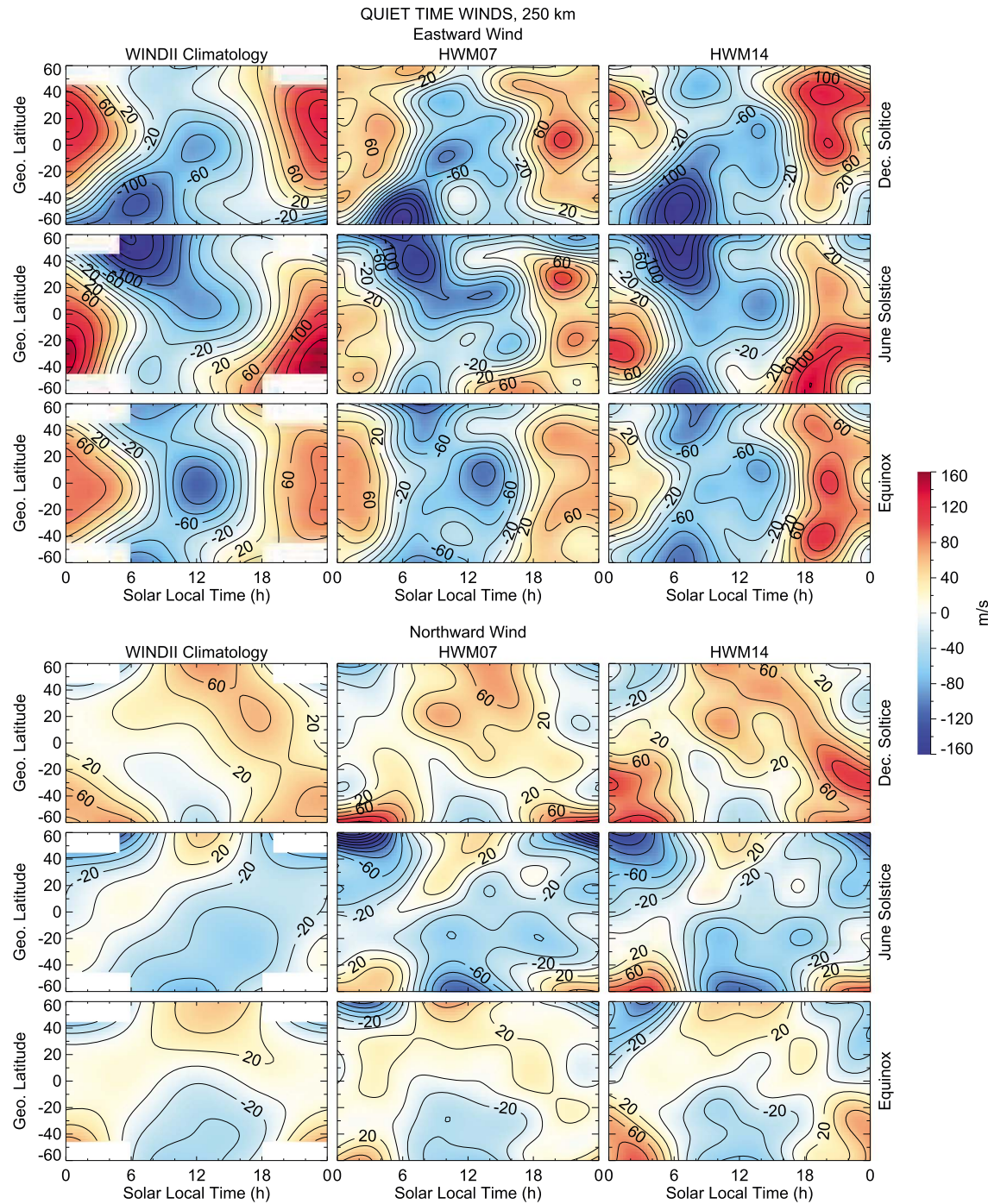


Figure 3. Zonal (top) and meridional (bottom) average quiet time ($K_p < 3$) winds at 250 km altitude, as a function of solar local time and geographic latitude. Shown are results from the quiet time (left) WINDII climatology of Emmert et al. [2002], (middle) HWM07, and (right) HWM14. The models were evaluated under December solstice (day of year 0), June solstice (day 180), and combined equinox (average of days 90 and 270) conditions, as indicated by the annotation at the right of each row.

$$W_n^l(\theta) = \frac{1}{\sqrt{n(n+1)}} \frac{m}{\cos(\theta)} P_n^l(\theta), \quad (6)$$

again, replacing $l \rightarrow m$ and $\delta \rightarrow \theta$ for the Ψ_j^3 functions. Additional details on equations (5) and (6) are provided by Swarztrauber [1993]. In HWM14, the functions are computed using the algorithm described by Emmert et al. [2010].

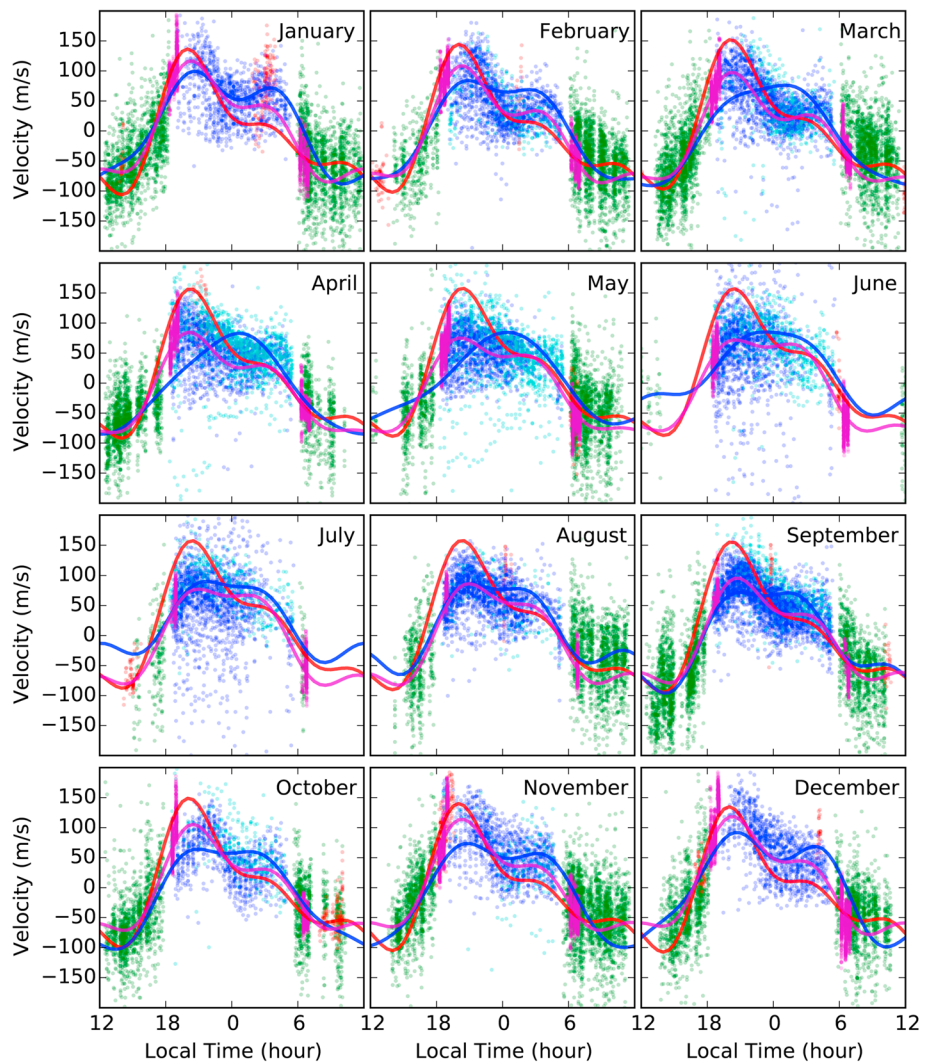


Figure 4. HWM comparisons with the zonal wind observations between 225 and 300 km within approximately $\pm 7.5^\circ$ latitude of the Relocatable Equatorial Nighttime Observatory of Ionospheric Regions (RENOIR) FPI (6.89°S , 38.56°W). The observations shown are from the RENOIR FPI (blue), Jicamarca FPI (cyan), GOCE satellite (magenta), WINDII 557.7-nm measurements (green), and DE2 WATS (red). The model results are HWM93 (red), HWM07 (blue), and HWM14 (magenta) at 250 km.

The unknown model coefficients C_r, C_i and B_r, B_i represent the real and imaginary parts of the vorticity and divergence of the vector wind field. The corresponding basis set for the meridional wind component $v_j(\tau, \delta, \theta, \phi)$ follows from the vector spherical harmonic coefficient parity relation: $u : \{C_r, C_i, B_r, B_i\} \leftrightarrow -v : \{B_r, B_i, -C_r, -C_i\}$. The linear basis for a line-of-sight wind w_{los} along a particular geographic bearing φ can be expressed as $w_{\text{los}} = u \sin \varphi + v \cos \varphi$.

2.3. Parameter Estimation

The entire set of unknown model parameters over the complete model domain $\mathbf{m} = \mathbf{m}_j^{(1)}, \dots, \mathbf{m}_{j+n}^{(3)}$ is estimated by solving an over-determined linear inverse problem $\mathbf{d} = \mathbf{G}\mathbf{m}$, where \mathbf{d} is the observation vector comprised of zonal, meridional, and line-of-sight wind measurements; and \mathbf{G} is a sparse stair step diagonal matrix given by equation (1). Each row of the forward matrix \mathbf{G} has nonzero support in four subcolumns of 800 elements each, corresponding to the basis functions $\beta_j u_j(\tau, \delta, \theta, \phi) + \dots + \beta_{j+3} u_{j+3}(\tau, \delta, \theta, \phi)$. Over the 30 vertical model level kernels j , there are a total of 24,000 unknown model coefficients in \mathbf{m} with the same number of columns in \mathbf{G} .

For HWM07, the parameters were estimated sequentially across submatrices with limited altitude support. In contrast, the entire set of HWM14 model parameters is now sequentially estimated across all altitude levels.

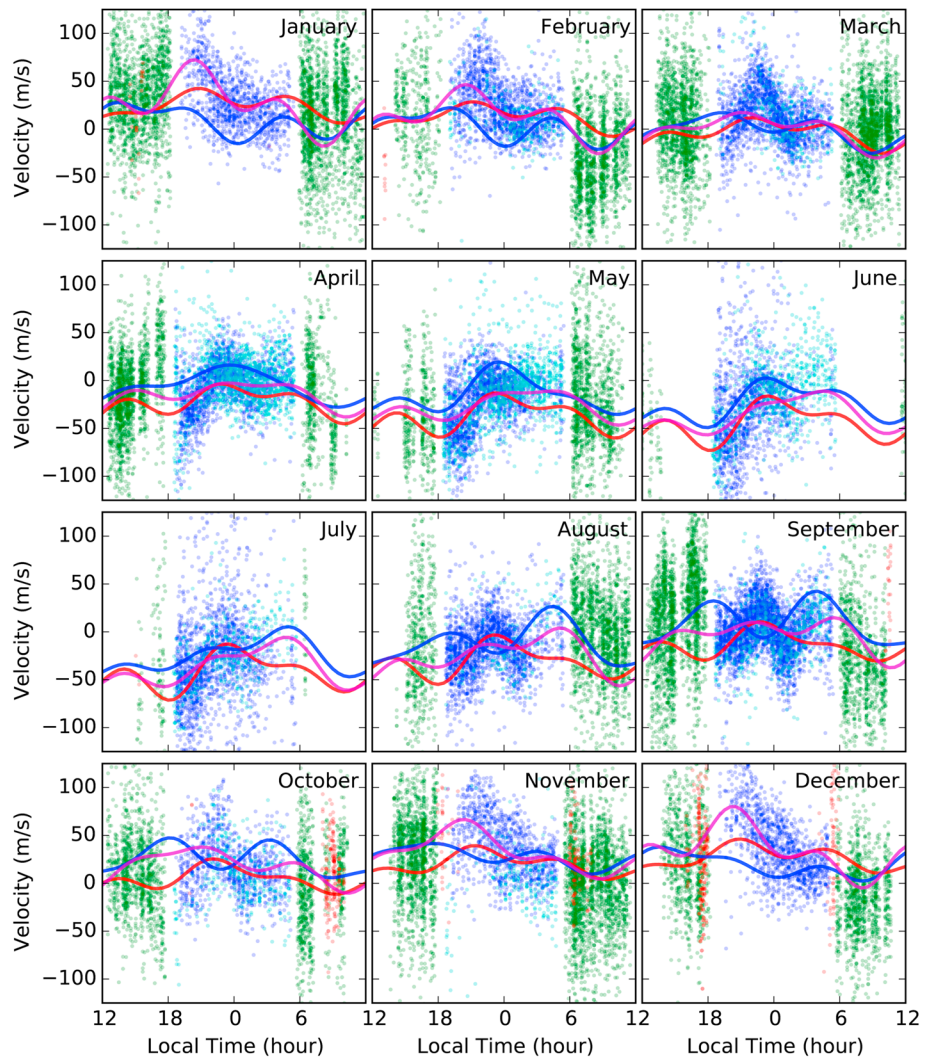


Figure 5. Same as Figure 4 but for the Meridional wind measurements and with the DE2 FPI observations (red).

This is achieved with the sparse Basic Linear Algebra Subprogram matrix library functions [Dongarra et al., 1990] and the iterative linear least squares optimal estimation procedure described by Rodgers [2000]. In this procedure the unknown model parameters are estimated via

$$\mathbf{m}_{n+1} = \mathbf{m}_n + [\mathbf{G}^T \mathbf{S}_e^{-1} \mathbf{G} + \mathbf{S}_n^{-1}]^{-1} \mathbf{G}^T \mathbf{S}_e [\mathbf{d} - \mathbf{G} \mathbf{m}_n] \quad (7)$$

$$\mathbf{S}_{n+1} = [\mathbf{G}^T \mathbf{S}_e^{-1} \mathbf{G} + \mathbf{S}_n^{-1}]^{-1}, \quad (8)$$

where at iteration $n + 1$ (not to be confused with model kernel level $j + 1$), \mathbf{m}_n is the prior estimate of all unknown model parameters, \mathbf{S}_n is the covariance matrix of the prior model parameters, and \mathbf{S}_e is the covariance matrix of the observations.

Parameter convergence is achieved after 10 iterations of $\sim 2 \times 10^6$ random samples (each) from the HWM observational database. Random sampling serves to evenly balance the various unevenly sampled data sets over space and time across the full model domain and to form a subset of the observations so that the forward matrix \mathbf{G} of each iteration can fit into available computer memory. Although measurement uncertainties are provided for each of the individual measurements (which range from ~ 10 to 60 m/s depending on the instrument), the observational covariance matrix is defined as $\mathbf{S}_e = \text{diag}[\|1/\sigma_i^2\|]$, where $\sigma_i = 37.5$ m/s. This is

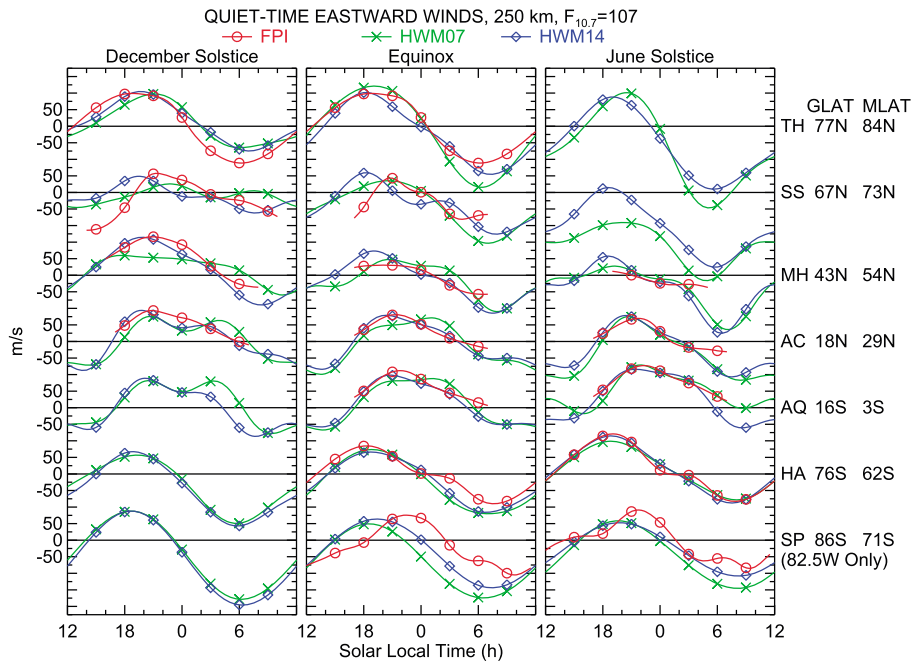


Figure 6. Comparison of average quiet time ($K_p < 3$) zonal winds as a function of local time from the site-specific FPI climatologies of Emmert et al. [2006a] (red circles), HWM07 (green crosses), and HWM14 (blue diamonds). The FPI models were evaluated for $F_{10.7} = 107$ sfu; results are shown for South Pole station (SP, 82.5°W longitude sector only), Halley (HA), Arequipa (AQ), Arecibo (AC), Millstone Hill (MH, north looking), Søndre Strømfjord (SS), and Thule (TH). The geographic and magnetic latitudes of each station are annotated on the right. (left) December solstice conditions (day of year 360), (middle) combined equinox (average of days 90 and 270), and (right) June solstice (day 180).

constant for all observations and chosen to reflect both the measurement uncertainties and the random geo-physical variability not representable by the empirical formulation. Data corresponding to geomagnetically quiet conditions (local 3 h $K_p < 3$) are used in the parameter estimation. The first iteration is started with \mathbf{m}_n and \mathbf{S}_n^{-1} equal to zero and performed using evenly distributed pseudo observations from both HWM93 and a multiyear TIEGCM model run. As described in Drob et al. [2008], these pseudo data are included as soft constraints in data-free regions to damp spurious artifacts toward reasonable values, thus making higher model resolution possible for the majority of the model space where observational coverage is good.

3. Results

This section describes main scientific results and key aspects of the model improvements. This includes overall statistical performance measures, specification of the thermospheric zonal mean general circulation, equatorial local-time variations, and the quiet time high-latitude circulation patterns.

3.1. Statistical Performance Measures

Two statistical metrics for the goodness of fit and model fidelity are model biases μ_q and root-mean-square error σ_q^{rms} . These measures are formally defined as

$$\mu_{q,j} = \frac{1}{N_j} \sum_{i=1}^{N_j} (d_i^o - d_i^q) \quad (9)$$

and

$$\sigma_{q,j}^{\text{rms}} = \sqrt{\frac{\sum_{i=1}^{N_j} (d_i^o - d_i^q)^2}{N_j}}, \quad (10)$$

for HWM versions $q = \{93, 07, 14\}$, where d_i^o is the i th observation of N_j total observations in data group j and d_i^q is model q 's estimate.

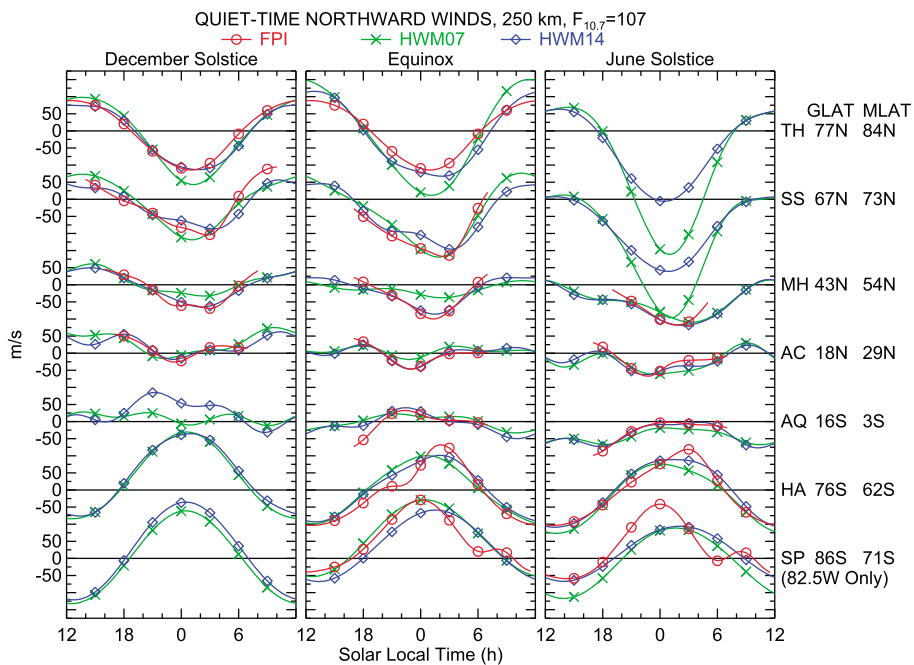


Figure 7. Same as Figure 6 but for the meridional component.

Table 2 shows the summary of these measures grouped by instrument and direction for all of the observations above 150 km utilized in the 10 iterations of equation (7). The unweighted sample mean μ_{obs} and standard deviation σ_{obs} for each group are also provided for comparison. The model with the worst performance is indicated in italics, and the model with the best performance is highlighted in bold. It is clear that HWM14 provides the best statistical representation of the observations of both the prior and new data sets.

3.2. Zonal Mean Circulation

The zonal mean structure of thermospheric zonal winds was first empirically described by Hedin *et al.* [1988, 1991]. This topic was recently revisited by Lieberman *et al.* [2013], who compared the diurnal average and migrating tides of longitudinally averaged zonal winds inferred from CHAMP accelerometer data [Liu *et al.*, 2006; Doornbos *et al.*, 2010] with results from the Whole Atmosphere Model (WAM) of Akmaev [2011]. This recent work highlights the value of HWM, which encapsulates an extensive and diverse database of observations for comparison with physics-based models.

Figure 2 shows the HWM longitudinally and diurnally averaged zonal winds at 300 km during different seasons. Similar to the results of Lieberman *et al.* [2013] for altitude between 350 and 400 km, a weak super rotation of ~ 10 m/s at the equator during December solstice conditions is observed, with strong westward winds of 60–100 m/s at 60° S in the summer hemisphere, and eastward zonal mean winds at 45° of ~ 30 m/s in the winter hemisphere. During equinox, HWM14 indicates only a marginal super rotation of no more than ~ 5 m/s at the equator, with the magnitude of the high-latitude westward winds reaches 30 m/s in both hemispheres.

One of the limitations of HWM14, and of the Lieberman *et al.* [2013] study, is the consideration of solar flux variation. The average $F_{10.7}$ of the data underlying HWM14 is 107 solar flux units ($1 \text{ sfu} = 10^{-22} \text{ W m}^{-2} \text{ Hz}^{-1}$) (sfu), and the average $F_{10.7}$ during the 2003–2007 period considered by Lieberman *et al.* [2013] is 89 sfu. For comparison in Figure 2 the corresponding results from HWM93 (that includes an $F_{10.7}$ effect parameterization) for $F_{10.7} = 90$ (dashed) and $F_{10.7} = 180$ (dotted) are also shown. For higher solar flux values HWM93 indicates a greater super rotation, exceeding 30 m/s at the equator. We note, however, that available zonal measurements in the equatorial region for HWM93 were limited. Only the DE2 WATS observations (with sparse day/night local time coverage during 2 years of solar maximum conditions) and the ground-based nighttime FPI measurements at Arequipa, Peru (16.5° S, 71.5° W), and Arecibo (18.3° N, 66.8° W) were available for HWM93 [Hedin *et al.*, 1991]. Analysis of equatorial CHAMP measurements by Liu *et al.* [2006], however, also indicates greater eastward momentum in the postdusk sector for increasing solar flux and greater westward momentum in the post midnight sector for decreasing solar flux (both in magnetic local time) implying a greater eastward

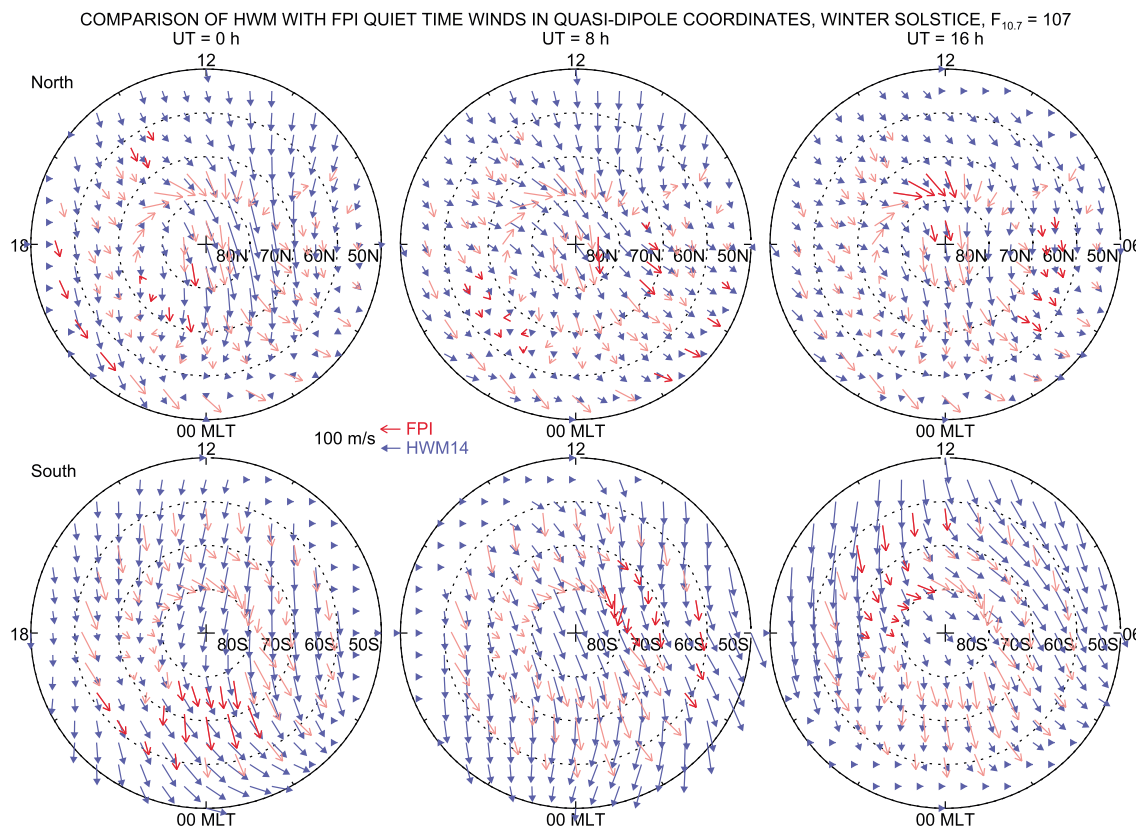


Figure 8. Average quiet time ($K_p < 3$) winter high-latitude circulation as a function of magnetic local time (MLT) and latitude derived from ground-based FPI measurements (red) and from HWM14 (blue). The FPI results are from the *Emmert et al.* [2006a, 2006b] climatologies and the Poker Flat Scanning Doppler Interferometer averaged in 1 h solar local time bins. (top) In the Northern Hemisphere the FPI measurements are Millstone Hill (north looking), Poker Flat (south looking), Poker Flat (north looking), Søndre Strømfjord, and Thule. (bottom) In the Southern Hemisphere the FPI results are from Halley Bay (37.5°W and 82.5°W) and South Pole (97.5°E and 142.5°E). All results are transformed into quasi-dipole coordinates [Richmond, 1995] in magnetic local time (MLT) and latitude. The HWM14 results are shown for 3 times (0, 8, and 16 UT) indicated at the top of each column. The MLT corresponding to each UT (± 1 h) is highlighted by the darker colored arrows.

momentum for larger solar flux conditions. Therefore, some caution is recommended when utilizing HWM14 above 250 km when $F_{10.7} > 150$. For the measurements in the HWM14 database the average, median, and modal values of $F_{10.7}$ are 107.08, 91.35, and 70.0 (± 0.5), respectively; biased toward solar minimum conditions. Interestingly, over the historical $F_{10.7}$ record from 1 January 1970 to 1 May 2014 (three full solar cycles) the average, median, and modal values are 122.4, 107.3, and 70.0 (± 0.5), respectively.

3.3. Equatorial Local Time Variations

Figure 3 compares the local time and latitude dependence of 250 km quiet time zonal and meridional winds from HWM14, HWM07, and the quiet time climatology of WINDII measurements described by *Emmert et al.* [2002]. Comparisons of these variations at lower altitudes are provided in the supporting information (Figures S1–S3). At 250 km altitude, the largest differences between HWM14 and HWM07 occur in the low-latitude and midlatitude postdusk sector. The nighttime differences are due in part to the inclusion of nighttime WINDII red line data in HWM07 but not in HWM14. Those data contain unexplained offsets associated with the satellite and instrument configuration [*Emmert et al.*, 2002]. These offsets apparently do not cancel out in the average low-latitude winds and contributed to the HWM07 discrepancies with ground-based measurements [*Meriwether et al.*, 2011; *Makela et al.*, 2013; *Huba et al.*, 2010] and herein.

The daytime HWM07 and HWM14 winds are generally in good agreement with the WINDII climatology, which provides the bulk of daytime upper thermospheric wind measurements in HWM. The finer structure of HWM is a result of its use of higher-order basis functions than the WINDII climatology, as well as additional data sets. The HWM14 zonal wind patterns are similar to the CHAMP-derived results shown in Figure 1 of *Lieberman et al.* [2013], except that the west-to-east reversal occurs at earlier local times in the higher altitude (350–400 km) CHAMP data. The HWM14 meridional wind tidal variations are much stronger than HWM07 and the WINDII

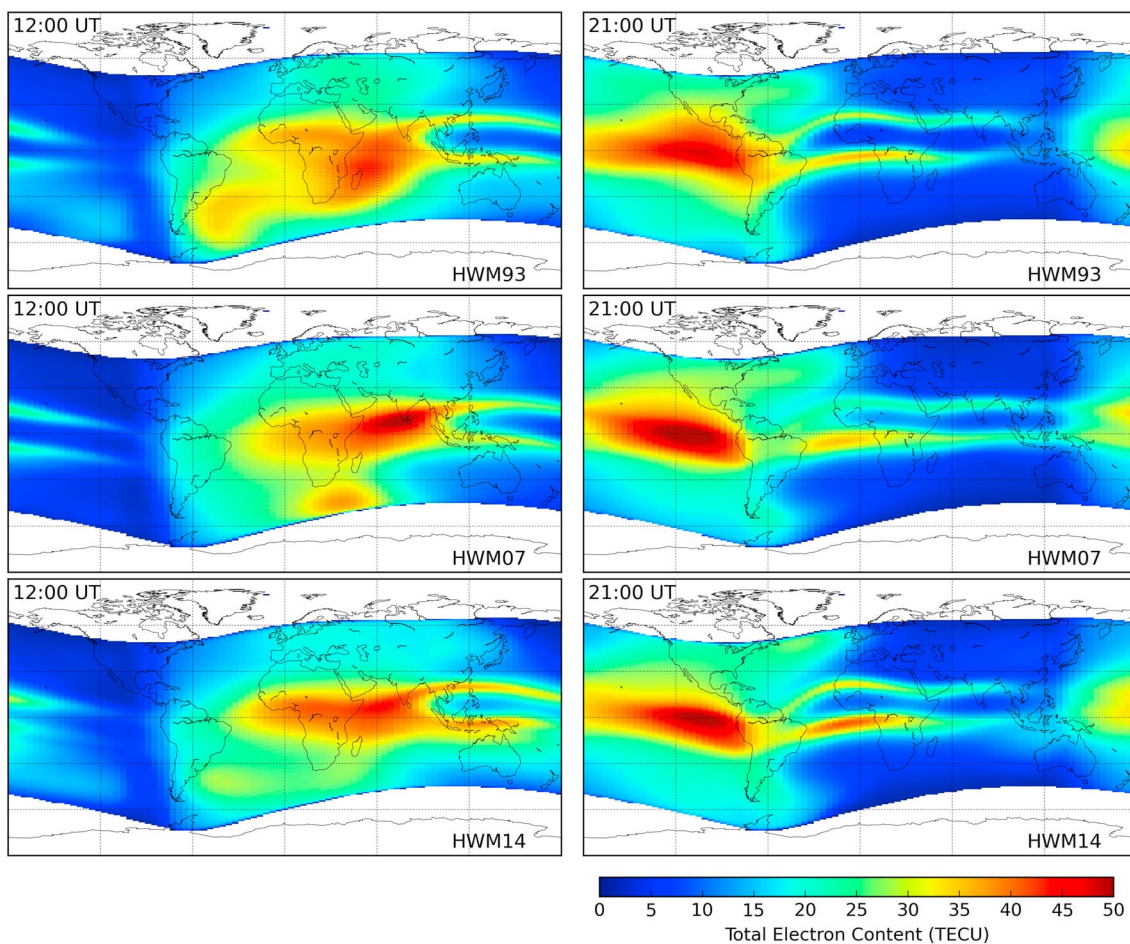


Figure 9. Comparison of the total electron content (TEC) computed with the SAMI3 model for day of year 80 (equinox) with $F_{10.7(a)} = 120$ at (left) 12:00 UT and (right) 21:00 UT from (top) HWM93, (middle) HWM07, and (bottom) HWM14.

climatology, particularly in the nighttime sector. This is primarily the result of the new ground-based FPI wind measurements as shown in subsequent figures.

One of the main reasons for updating HWM was to correct problems with the equatorial zonal wind local time variations. Figure 4 shows a comparison of the individual zonal wind observations between 225 and 300 km within approximately $\pm 7.5^\circ$ latitude of the Relocatable Equatorial Nighttime Observatory of Ionospheric Regions (RENOIR) FPI (6.89°S , 38.56°W). The observations from the RENOIR FPI (blue), Jicamarca FPI (cyan), GOCE satellite (magenta), WINDII 557.7 nm measurements (green), and DE2 WATS instrument (red) are shown. The latitude selection criteria is slightly relaxed to include all of the Jicamarca observations (11.96°S , 76.86°W). Observations at all longitudes are included from the DE2 WATS instrument, but only within $\pm 90.0^\circ$ longitude from WINDII, and $\pm 10.0^\circ$ from GOCE. The individual data points are shown in order to highlight the day-to-day variability discussed in the introduction, as well as the sampling density of the observations. Not shown are the reported measurement uncertainties which can vary from ~ 10 to 60 m/s depending on the instrument.

There is general consensus among the various data sets where they overlap and/or are adjacent. The interannual self-consistency of local time variations is demonstrated by the fact that the DE2 observations were obtained from 1981 to 1983, the WINDII observation between 1992 and 1997, the GOCE measurements from 2009 to 2012, and FPI measurement from 2009 to 2013. The DE2 WATS measurements are generally biased high. The average of the hourly standard deviations for all of the data shown is 36.7 m/s. To a crude approximation from the relation $\sigma_{\text{net}}^2 = \sigma_{\text{geo}}^2 + \sigma_{\text{obs}}^2$, and assuming an average range of measurement uncertainties from ~ 15 to 30 m/s, the variability attributable to geophysical origins is ~ 26.3 to 34.4 m/s.

Table 3. Comparison of the Absolute Difference (μ) and Standard Deviation (σ) of Computed Vertical Ion Drifts From SAMI3/HWM [McDonald *et al.*, 2014] and the Scherliess-Fejer Empirical Vertical Drift Model [Scherliess and Fejer, 1999] Over Longitude and Local Time for a Given Day^a

Day of Year	μ_{93}	μ_{07}	μ_{14}	σ_{93}	σ_{07}	σ_{14}
001	10.4	8.7	8.0	7.3	5.9	4.8
091	10.1	8.9	7.1	7.6	4.8	4.0
182	10.8	11.0	9.2	7.8	6.3	4.8
274	10.2	8.9	7.6	7.7	5.2	4.4

^aThe best and the worst scores are denoted in bold and italics, respectively.

Empirical model results from HWM93 (red), HWM07 (blue), and HWM14 (magenta) at 250 km for each month are also shown in Figure 4. A constant $F_{10.7}$ value of 107 sfu is assumed for the HWM93 calculations. HWM14 appears to adequately represent the mean of the data. Not surprisingly it is more accurate than HWM07 or HWM93 as only HWM14 was fit with these particular data. HWM93 overestimates the observed eastward maximum occurring just after dusk between 18:00 and 21:00 LT. HWM93 and results by Biondi *et al.* [1999], Emmert *et al.* [2006a], and Liu *et al.* [2006] all indicate that the magnitude of this maximum increases with solar flux, by about 25 m/s from solar minimum to solar maximum. However, HWM93 exceeds the data shown in Figure 4 by more than 50 m/s, so the different $F_{10.7}$ sampling by HWM93 and HWM14 cannot explain this discrepancy. The CHAMP results of Liu *et al.* [2006] indicate that the average postdusk peak near 400 km is 150 to 170 m/s, similar to the HWM93 results. Issues related to the altitude dependence of the thermospheric winds in HWM is discussed later in section 4.2.

By contrast, HWM07 underestimates and even completely misses the postsunset feature (see in Figure 4), primarily as a result of the influence of nighttime 630 nm WINDII observations as discussed above. This is believed to be the reason for the difficulties encountered by Huba *et al.* [2009] in predicting the eastward drift rate of equatorial plasma bubbles using HWM07 as compared to HWM93.

Figure 5 shows the corresponding meridional wind measurements at this location. DE2 630 nm FPI measurements (red) replace the DE2 WATS. There is a reasonable consensus between the various measurements in the climatological sense again. HWM14 appears to provide the best representation of the data, particularly during November through January. During the equinox months of March and September, however, the agreement with the observations is only slightly better. None of the models resolve the 50 m/s northward excursion seen in the Renoir data just after 21:00 local time (–3:00 LT) during March and September. Additional research is needed to understand and resolve this feature.

3.4. Comparison to FPI Climatologies, Including High Latitudes

This section compares HWM07 and HWM14 with the quiet time climatologies of ground-based FPI data described by Emmert *et al.* [2006a, 2006b]. Again, the site-specific FPI models are evaluated for $F_{10.7} = 107$ sfu. The quiet time criterion is the same for all of these models; local 3-hour $K_p < 3$. The local time and seasonal dependence and the high-latitude circulation are described.

Figure 6 summarizes the local time dependence of the FPI and HWM zonal winds. HWM14 is in better agreement with the FPI models than HWM07, except for the Søndre Strømfjord FPI. In this case, HWM14 may be influenced by the Poker Flat observations, which are from a slightly lower latitude than Søndre Strømfjord and which were not included in HWM07. The improvement in the agreement with equatorial FPI winds discussed above is evident in the comparison with the Arequipa climatology and extends to the low-latitude and midlatitude locations of Arecibo and Millstone Hill. Figure 7 shows the corresponding meridional winds. HWM14 is in better agreement with the FPI models than HWM07, except for the equinox winds measured from the South Pole along the 82.5°W meridian.

Figure 8 compares the quiet time winter high-latitude circulation in HWM14 with the Emmert *et al.* [2006a] FPI climatologies. Also shown are quiet time ($K_p < 3$) winds from the Poker Flat Scanning Doppler Interferometer (SDI) averaged in 1 h solar local time bins and two latitude bands (north of the station and south of the station). All results are transformed into quasi-dipole apex coordinates [Richmond, 1995] as a function of magnetic local time and latitude as described in Emmert *et al.* [2006b]. The HWM14 results are shown at three universal times (0:00, 8:00, and 16:00 UT). For each FPI the magnetic local times within 1 h of each UT are highlighted

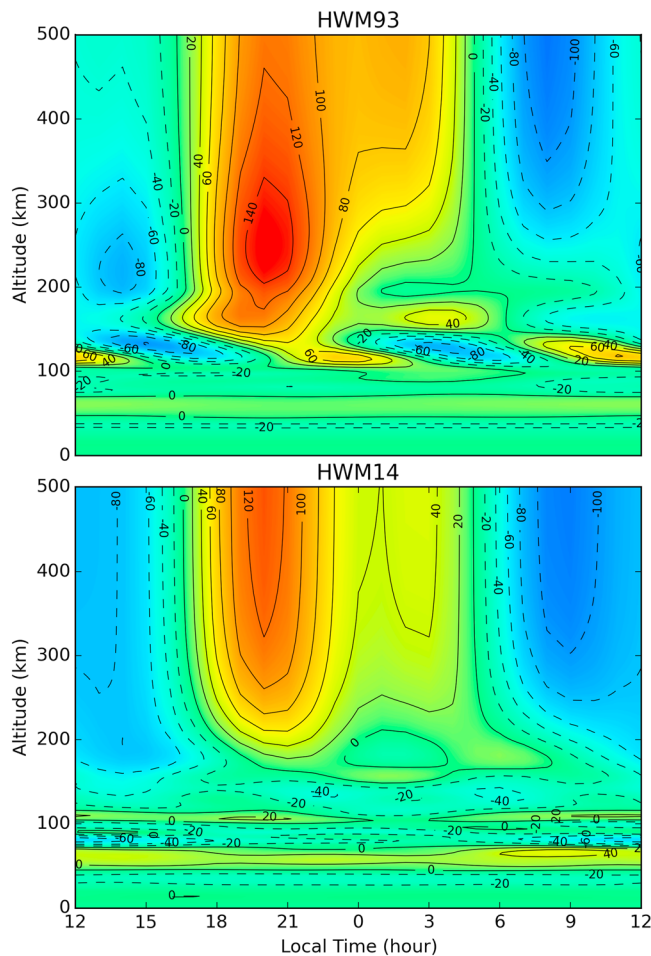


Figure 10. Comparison of the zonal wind profiles as a function of altitude and local time for (top) HWM93 and (bottom) HWM14 at RENOIR (6.89°S , 38.56°W) during equinox conditions (day of year 81). For HWM93 $F_{10.7} = 107$.

by the darker colored arrows. At these magnetic local times the comparison between HWM14 and the FPI climatologies are the most direct.

The agreement between HWM14 and the FPI results is fair to good, but the best agreement does not always occur at the coincident magnetic local times. HWM14 shows the expected strong antisunward flow, but the fingerprints of ion convection are not evident. As noted by *Emmert et al.* [2006b], the effect of ion convection is not very noticeable in the winter quiet time FPI winds, while under geomagnetically disturbed conditions, the two-cell convection pattern is quite prominent [*Emmert et al.*, 2008]. For the universal times chosen, the observed differences between HWM14 (and the FPI observations) between the Northern Hemisphere December solstice and the Southern Hemisphere June solstice are related to the offset between the geomagnetic pole and the location of the day-night terminator in universal time. Difficulty representing the influence of the high-latitude ionospheric convection pattern with the present model formulation is briefly described later.

4. Discussion

4.1. Self-Consistency of Ionosphere Structures

The HWM provides drivers for first principles ionospheric models [e.g., *Alken and Maus*, 2010; *Huba et al.*, 2010]. To illustrate the effect of the updates to HWM on ionospheric specifications, calculations of the total electron content (TEC) by the NRL ionosphere model SAMI3 [*Huba et al.*, 2000, 2010] with three different versions of wind climatology are shown in Figure 9. These calculations also use the quasi-dipole apex magnetic model of *Richmond* [1995]. The geophysical conditions for the simulations are $F_{10.7} = 120$, $A_p = 3$ and day of year 80 (equinox). Model outputs for 12:00 UT (left) and 21:00 UT (right) are shown. Comparisons with observed

global TEC maps [e.g., Yasyukevich *et al.*, 2010; Jee *et al.*, 2014] are beyond the scope of this paper and left to the reader.

The computed TEC for the three wind models are typical of observations and similar to each other but there are some noteworthy differences, particularly at 12:00 UT. For example, the anomalous features seen in the Southern Atlantic Ocean (near South America) for HWM93, and off the Cape of Africa for HWM07 (at 12:00 UT) are not present in the HWM14 results. At 21:00 UT the daytime longitudinal extent of $\text{TEC} > 35 \text{ TECU}$ ($1 \text{ TECU} = 1 \times 10^{16} \text{ electrons/m}^2$) for HWM07 is narrower than that of HWM93 and HWM14. There is also a larger TEC in the daytime, mid-latitude with HWM93 as compared to HWM07 and HWM14, especially in the southern hemisphere afternoon sector. Lastly, there is an eastward shift in the northern hemisphere TEC relative to HWM93 and HWM07. These differences in TEC are largely attributed to differences in the specification of the meridional wind.

A second means to validate the improvement to HWM in the context of first-principles ionospheric calculations is to compute the self-consistent vertical $\mathbf{E} \times \mathbf{B}$ drifts and compare those to the empirical vertical drift model of Scherliess and Fejer [1999]. For these calculations SAMI3 is run for the geophysical conditions in 2009 for day numbers 1, 91, 198, and 271. The corresponding values for $F_{10.7}$ are all less than 72 sfu. Additional detail regarding these calculations is provided by McDonald *et al.* [2014]. Table 3 shows a comparison via the average bias (μ) and root-mean-square standard deviation (σ) of computed vertical ion drifts from SAMI3/HWM and the Scherliess-Fejer empirical vertical drift model. Each metric is calculated over all longitudes and local times for a given day. For these metrics HWM14 produces the best results (**bold**) and HWM93 the worst results (*italics*), while overall, the equinox months showed better agreement than solstice months.

4.2. Limitations and the Way Forward

One missing component of HWM14 is a solar flux parameterization. Comparisons between theoretical models and available observations [Biondi *et al.*, 1999; Liu *et al.*, 2010; Emmert *et al.*, 2006a] indicate that the solar flux dependence of the local time behavior of equatorial region zonal winds is not yet completely understood. The uneven sampling distribution of the HWM database makes incorporation of a reliable solar flux dependence very difficult, but recent observations not yet included in the model, such as from CHAMP, may alleviate this difficulty. An accurate characterization of the solar flux dependence of thermospheric winds would help constrain first-principles models of thermospheric dynamics, especially with respect to ion-neutral coupling.

Another long-standing problem that is hampered by a lack of suitable measurements is knowledge of the vertical variations of the horizontal winds in the upper thermosphere above 250 km. Most theoretical models, as well as HWM, assume that above some nominal altitude (typically 300 to 450 km) or as an upper boundary condition, the vertical gradient of the horizontal winds becomes zero, i.e., $du/dz = 0$, $dv/dz = 0$. This topic was recently investigated with the TIEGCM in the context of geomagnetic storms by Wang *et al.* [2008] but has received very little attention in terms of quiet time thermospheric dynamics. This issue has important consequences for the mapping of in situ winds measured at altitude near 400 km downward to F region altitudes near 250 km to support ionospheric data assimilation systems.

Figure 10 shows a comparison of the vertical profiles of HWM93 and HWM14 zonal wind as a function of local time (LT) at the location of the RENOIR FPI (6.89°S , 38.56°W) for equinox conditions (day 81) with $F_{10.7} = 107$ in HWM93. There are substantive differences. First the anomalous zonal wind component of the westward semidiurnal migrating tide in the lower thermosphere, known from observations and theory to have a minimum at equatorial latitudes [e.g., Oberheide *et al.*, 2011], was corrected in HWM07 [Drob *et al.*, 2008]. At F region altitudes, HWM93 has a westward peak wind between noon (12:00 LT) and sunset (6:00 LT) of approximately -80 m/s increasing above to approximately -40 m/s near 400 km. Between sunset (6:00 LT) and midnight (0:00 LT), HWM93 indicates an eastward peak wind of 140 m/s near 250 km decreasing to 120 m/s above. By contrast HWM14 winds have no inflection points above about 200 km and reach similar constant values of -80 m/s and 120 m/s , respectively, at $\sim 400 \text{ km}$.

Early theoretical studies indicate that during solar maximum conditions inflection points may occur as the result of ion drag, whereas during solar minimum condition the thermospheric winds should be constant above about 250 km. HWM93 does include a solar flux parametrization in the form of a polynomial multiplier dependent on $F_{10.7}$ with changing vertical gradients in the zonal winds above 300 km. In contrast, HWM14 does not yet contain a solar flux parametrization and has nearly constant zonal winds above about 350 km. While this is a limitation of HWM14, the parameterization used in HWM93 is fairly simple and has

not been validated. In addition, the vertical structure exhibited by HWM14 is inline with the fact that CHAMP post sunset peak wind amplitudes near 400 km are ~50 m/s greater than the local time variations observed by ground-based 630 nm wind measurements for altitude of 250 km. In order to solve this problem, both measurements from higher solar flux conditions and particularly measurements of the vertical profile of the neutral winds are required.

Furthermore, despite almost 50 years of space research there are also altitude regions where the thermospheric winds have not been routinely measured, such as nighttime conditions from 120 to 200 km. Advanced thermospheric wind measurement techniques such as *Hysell et al.* [2014], and the planned instruments on the upcoming NASA Ionosphere Connection mission may partially fill the former gap, but not the latter. From this work it is also clear that continued operation of existing ground-based FPIs, as well as the deployment in under sampled geographic regions will improve scientific understanding. Furthermore, the development of techniques to provide 24 h of continuous coverage would be very useful, as well as common volume networks to resolve divergence and curl. The utility of cross-track winds derived from satellite accelerometer measurements is also obvious.

Lastly, the differences between the quiet time HWM14 and FPI high-latitude winds highlight the difficulty, described by *Emmert et al.* [2010] of representing high-latitude circulation in geographic coordinates, especially in winter, when few satellite-based measurements are available to provide the longitudinal dependence needed to describe a system that is primarily organized in geomagnetic coordinates. The high-latitude circulation in HWM14 could be improved by incorporating coupled longitude-local time variations (i.e., nonmigrating tides) or by transitioning from a geographic to geomagnetic basis at high latitudes.

5. Conclusion

Thirty years of HWM empirical model development has shown that to properly resolve the thermospheric wind patterns the utilization of both satellite and ground-based data sets is essential. In the future this will also become important for assimilative real-time meteorological forecast models that include the thermosphere. As the heliophysics community works toward real-time thermospheric data assimilation, it is important not to lose sight of historical data sets. There are both agreements and discrepancies between first-principles models and the observational data sets, as well as between the various observational data sets themselves. The identification and resolution of these discrepancies is fundamentally important, and empirical models like HWM play a critical role in this activity.

The horizontal wind model (HWM) has been updated in the thermosphere with satellite- and ground-based observations, as well as improvements to the parameter estimation procedures and the model formulation. New ground-based 630 nm Fabry-Perot Interferometer (FPI) measurements, along with the cross-track wind measurements from the GOCE satellite fill important gaps in both latitude and local time coverage. Where the observations overlap and/or are adjacent in space and time, the construction of this reference model provided the opportunity to validate these new measurements in the climatological sense. For the data sets shown, there do not appear to be any climatological discrepancies among each other.

The resulting HWM14 provides an improved time dependent, observationally based, global empirical specification of the upper atmospheric tides and general circulation patterns. Already in line with existing accepted theoretical knowledge of the thermosphere general circulation, ionospheric simulations indicate that the winds in HWM14 are consistent with climatological ionosphere plasma distribution and electric fields. The update provides an improved specification of thermospheric general circulation to support both scientific and space weather applications. The HWM14 end-user FORTRAN-90 subroutines and coefficient files are available in the online supporting information.

References

- Akmaev, R. (2011), Whole atmosphere modeling: Connecting terrestrial and space weather, *Rev. Geophys.*, 49, RG4004, doi:10.1029/2011RG000364.
Alken, P., and S. Maus (2010), Electric fields in the equatorial ionosphere derived from CHAMP satellite magnetic field measurements, *J. Atmos. Sol. Terr. Phys.*, 72(4), 319–326, doi:10.1029/2008GL033580.
Biondi, M., S. Sazykin, B. G. Fejer, J. Meriwether, and C. Fesen (1999), Equatorial and low latitude thermospheric winds: Measured quiet time variations with season and solar flux from 1980 to 1990, *J. Geophys. Res.*, 104(A8), 17,091–17,106, doi:10.1029/1999JA900174.
Buonsanto, M., J. Salah, K. Miller, W. Oliver, R. Burnside, and P. Richards (1989), Observations of neutral circulation at mid-latitudes during the equinox transition study, *J. Geophys. Res.*, 94(A12), 16,987–16,997, doi:10.1029/JA094iA12p16987.

Acknowledgments

This paper is dedicated to the memory of Gonzalo Hernandez. D.P. Drob, J.T. Emmert, S.D. McDonald, K.A. Zawdie, and J.D. Huba acknowledge support from the Chief of Naval Research (CNR) as part of the Integrated Sun-Earth System for the Operational Environment (ISES-OE) project under the NRL base program. J.N. would like to acknowledge B. Kerr for development of the data analysis schema for the next-generation Arecibo FPI observations. J.D.H. would like to acknowledge Gang Lu at the High Altitude Observatory (HAO) of the National Center for Atmospheric Research (NCAR) for inclusion of the quasi-dipole apex magnetic coordinate system model in SAMI3. The ground-based FPI wind data sets are available from the MADRIGAL database (<http://cedar.openmadrigal.org>), which is supported by the National Science Foundation (NSF). The GOCE thermosphere data are available from ESA (<https://earth.esa.int/web/guest/-/goce-data-access-7219>). GOCE thermosphere data processing was supported by ESAs Support-To-Science Element. The NASA mission data are available from <http://spdf.gsfc.nasa.gov> and <http://disc.sci.gsfc.nasa.gov>.

- Burnside, R., and C. Tepley (1989), Optical observations of thermospheric neutral winds at Arecibo between 1980 and 1987, *J. Geophys. Res.*, 94(A3), 2711–2716, doi:10.1029/JA094iA03p02711.
- Conde, M., and R. Smith (1995), Mapping thermospheric winds in the auroral zone, *Geophys. Res. Lett.*, 22(22), 3019–3022, doi:10.1029/95GL02437.
- Conde, M., and R. Smith (1998), Spatial structure in the thermospheric horizontal wind above Poker Flat, Alaska, during solar minimum, *J. Geophys. Res.*, 103(A5), 9449–9471, doi:10.1029/97JA03331.
- Daley, R. (1993), Atmospheric Data Analysis, 2.
- Dongarra, J. J., J. D. Croz, S. Hammarling, and I. S. Duff (1990), A set of level 3 basic linear algebra subprograms, *ACM Trans. Math. Soft.*, 16(1), 1–17, doi:10.1145/77626.79170.
- Doornbos, E., J. van den IJssel, H. Lühr, M. Förster, and G. Koppenwallner (2010), Neutral density and crosswind determination from arbitrarily oriented multiaxis accelerometers on satellites, *J. Spacecraft Rockets*, 47(4), 580–589, doi:10.2514/1.48114.
- Doornbos, E., S. Bruinsma, S. Fritzsche, G. Koppenwallner, P. Visser, J. van den IJssel, and J. de Teixeira da Encarnacao (2014), GOCE+ theme 3: Air density and wind retrieval using GOCE data final report, *Tech. Rep. 4000102847/NL/EL*, TU Delft, Netherlands.
- Drob, D., et al. (2008), An empirical model of the Earth's horizontal wind fields: HWM07, *J. Geophys. Res.*, 113, A12304, doi:10.1029/2008JA013668.
- Drob, D. P., R. Meier, J. M. Picone, and M. M. Garcés (2009), Inversion of infrasound signals for passive atmospheric remote sensing, in *Infrasound Monitoring for Atmospheric Studies*, edited by A. L. Pichon, E. Blanc and A. Hauchecorne, pp. 701–731, Springer, Netherlands, doi:10.1007/978-1-4020-9508-5_24.
- Emmert, J., B. G. Fejer, G. Shepherd, and B. Solheim (2002), Altitude dependence of middle and low-latitude daytime thermospheric disturbance winds measured by WINDII, *J. Geophys. Res.*, 107(A12), 1483, doi:10.1029/2002JA009646.
- Emmert, J., M. Faivre, G. Hernandez, M. Jarvis, J. Meriwether, R. Niciejewski, D. Sipler, and C. Tepley (2006a), Climatologies of nighttime upper thermospheric winds measured by ground-based Fabry-Perot interferometers during geomagnetically quiet conditions: 1. local time, latitudinal, seasonal, and solar cycle dependence, *J. Geophys. Res.*, 111, A12302, doi:10.1029/2006JA011948.
- Emmert, J., G. Hernandez, M. Jarvis, R. Niciejewski, D. Sipler, and S. Vennerstrom (2006b), Climatologies of nighttime upper thermospheric winds measured by ground-based Fabry-Perot interferometers during geomagnetically quiet conditions: 2. high-latitude circulation and interplanetary magnetic field dependence, *J. Geophys. Res.*, 111, A12303, doi:10.1029/2006JA011949.
- Emmert, J., D. Drob, G. Shepherd, G. Hernandez, M. J. Jarvis, J. Meriwether, R. Niciejewski, D. Sipler, and C. Tepley (2008), DWM07 global empirical model of upper thermospheric storm-induced disturbance winds, *J. Geophys. Res.*, 113, A11319, doi:10.1029/2008JA013541.
- Emmert, J., A. Richmond, and D. Drob (2010), A computationally compact representation of magnetic-apex and quasi-dipole coordinates with smooth base vectors, *J. Geophys. Res.*, 115, A08322, doi:10.1029/2010JA015326.
- Fang, T.-W., R. Akmaev, T. Fuller-Rowell, F. Wu, N. Maruyama, and G. Millward (2013), Longitudinal and day-to-day variability in the ionosphere from lower atmosphere tidal forcing, *Geophys. Res. Lett.*, 40(11), 2523–2528, doi:10.1002/grl.50550.
- Fuller-Rowell, T. J., and D. Rees (1980), A three-dimensional time-dependent global model of the thermosphere, *J. Atmos. Sci.*, 37(11), 2545–2567, doi:10.1175/1520-0469(1980)037<2545:ATDTDG>2.0.CO;2.
- Geisler, J. (1967), A numerical study of the wind system in the middle thermosphere, *J. Atmos. Terr. Phys.*, 29(12), 1469–1482, doi:10.1016/0021-9169(67)90100-6.
- Hays, P., J. Meriwether, and R. Roble (1979), Nighttime thermospheric winds at high latitudes, *J. Geophys. Res.*, 84(A5), 1905–1913, doi:10.1029/JA084iA05p01905.
- Hays, P., T. Killeen, and B. Kennedy (1981), The Fabry-Perot Interferometer on dynamics explorer, *Space Sci. Instrum.*, 5, 395–416.
- Hedin, A. E. (1987), MSIS-86 thermospheric model, *J. Geophys. Res.*, 92(A5), 4649–4662, doi:10.1029/JA092iA05p04649.
- Hedin, A. E., N. Spencer, and T. Killeen (1988), Empirical global model of upper thermosphere winds based on atmosphere and dynamics explorer satellite data, *J. Geophys. Res.*, 93(A9), 9959–9978, doi:10.1029/JA093iA09p09959.
- Hedin, A. E., et al. (1991), Revised global model of thermosphere winds using satellite and ground-based observations, *J. Geophys. Res.*, 96(A5), 7657–7688, doi:10.1029/91JA00251.
- Hernandez, G., and R. Roble (1976), Direct measurements of nighttime thermospheric winds and temperatures: 1. Seasonal variations during geomagnetic quiet periods, *J. Geophys. Res.*, 81(13), 2065–2074, doi:10.1029/JA081i013p02065.
- Hernandez, G., R. Smith, and J. Conner (1992), Neutral wind and temperature in the upper mesosphere above South Pole, Antarctica, *Geophys. Res. Lett.*, 19(1), 53–56, doi:10.1029/91GL02957.
- Huba, J., G. Joyce, and J. Fedder (2000), Sami2 is another model of the ionosphere (SAMI2): A new low-latitude ionosphere model, *J. Geophys. Res.*, 105(A10), 23,035–23,053, doi:10.1029/2000JA000035.
- Huba, J., S. Ossakow, G. Joyce, J. Krall, and S. England (2009), Three-dimensional equatorial spread F modeling: Zonal neutral wind effects, *Geophys. Res. Lett.*, 36, L19106, doi:10.1029/2009GL040284.
- Huba, J., G. Joyce, J. Krall, C. Siefring, and P. Bernhardt (2010), Self-consistent modeling of equatorial dawn density depletions with SAMI3, *Geophys. Res. Lett.*, 37, L03104, doi:10.1029/2009GL041492.
- Hysell, D., M. Larsen, and M. Sulzer (2014), High time and height resolution neutral wind profile measurements across the mesosphere/lower thermosphere region using the Arecibo incoherent scatter radar, *J. Geophys. Res. Space Physics*, 119, 2345–2358, doi:10.1002/2013JA019621.
- Jacchia, L. G. (1965), *Static Diffusion Models of the Upper Atmosphere With Empirical Temperature Profiles*, Smithsonian Contrib. to Astrophys., vol. 215, Smithsonian Institution, Washington, D. C.
- Jee, G., H. Lee, and S. Solomon (2014), Global ionospheric total electron contents (TECs) during the last two solar minimum periods, *J. Geophys. Res. Space Physics*, 119, 2090–2100, doi:10.1002/2013JA019407.
- Jin, H., Y. Miyoshi, H. Fujiwara, H. Shinagawa, K. Terada, N. Terada, M. Ishii, Y. Otsuka, and A. Saito (2011), Vertical connection from the tropospheric activities to the ionospheric longitudinal structure simulated by a new Earth's whole atmosphere-ionosphere coupled model, *J. Geophys. Res.*, 116, A01316, doi:10.1029/2010JA015925.
- Kelly, M., J. Comberiate, E. Miller, and J. Paxton (2014), Progress toward forecasting of space weather effects on UHF SATCOM after Operation Anaconda, *Space Weather*, 12, 601–611, doi:10.1002/2014SW001081.
- Killeen, T. (1987), Energetics and dynamics of the Earth's thermosphere, *Rev. Geophys.*, 25(3), 433–454, doi:10.1029/RG025i003p00433.
- Killeen, T., Q. Wu, S. Solomon, D. Orton, W. Skinner, R. Niciejewski, and D. Gell (2006), TIMED Doppler interferometer: Overview and recent results, *J. Geophys. Res.*, 111, A10S01, doi:10.1029/2005JA011484.
- Killeen, T. L., P. Hays, N. W. Spencer, and L. Wharton (1982), Neutral winds in the polar thermosphere as measured from dynamics explorer, *Geophys. Res. Lett.*, 9(9), 957–960, doi:10.1029/GL009i009p00957.
- Kohl, H., and J. King (1967), Atmospheric winds between 100 and 700 km and their effects on the ionosphere, *J. Atmos. Terr. Phys.*, 29(9), 1045–1062, doi:10.1016/0021-9169(67)90139-0.

- Lieberman, R., R. Akmaev, T. Fuller-Rowell, and E. Doornbos (2013), Thermospheric zonal mean winds and tides revealed by CHAMP, *Geophys. Res. Lett.*, 40, 2439–2443, doi:10.1002/grl.50481.
- Liu, H., H. Lühr, S. Watanabe, W. Köhler, V. Henize, and P. Visser (2006), Zonal winds in the equatorial upper thermosphere: Decomposing the solar flux, geomagnetic activity, and seasonal dependencies, *J. Geophys. Res.*, 111, A07307, doi:10.1029/2005JA011415.
- Liu, H.-L., et al. (2010), Thermosphere extension of the whole atmosphere community climate model, *J. Geophys. Res.*, 115, A12302, doi:10.1029/2010JA015586.
- Lühr, H., S. Rentz, P. Ritter, H. Liu, and K. Häusler (2007), Average thermospheric wind patterns over the polar regions, as observed by CHAMP, *Ann. Geophys.*, 25, 1093–1101.
- Makela, J. J., J. W. Meriwether, A. J. Ridley, M. Ciocca, and M. W. Castellez (2012), Large-scale measurements of thermospheric dynamics with a multisite Fabry-Perot interferometer network: Overview of plans and results from midlatitude measurements, *Int. J. Geophys.*, 2012, 1–10, doi:10.1155/2012/872140.
- Makela, J. J., D. J. Fisher, J. W. Meriwether, R. A. Buriti, and A. F. Medeiros (2013), Near-continual ground-based nighttime observations of thermospheric neutral winds and temperatures over equatorial Brazil from 2009 to 2012, *J. Atmos. Sol. Terr. Phys.*, 103, 94–102, doi:10.1016/j.jastp.2012.11.019.
- McDonald, S., J. Lean, J. Huba, G. Joyce, J. Emmert, and D. Drob (2014), Long-term simulations of the ionosphere using SAMI3, in *Modeling the Ionosphere-Thermosphere System*, edited by J. Huba, R. Schunk, and G. Khazanov, pp. 119–131, John Wiley, Chichester, U.K., doi:10.1029/2012GM001301.
- Mendillo, M., H. Rishbeth, R. Roble, and J. Wroten (2002), Modelling F2-layer seasonal trends and day-to-day variability driven by coupling with the lower atmosphere, *J. Atmos. Sol. Terr. Phys.*, 64(18), 1911–1931, doi:10.1016/S1364-6826(02)00193-1.
- Meriwether, J., M. Faivre, C. Fesen, P. Sherwood, and O. Veliz (2008), New results on equatorial thermospheric winds and the midnight temperature maximum, *Ann. Geophys.*, 26, 447–466.
- Meriwether, J., J. Makela, Y. Huang, D. Fisher, R. Buriti, A. Medeiros, and H. Takahashi (2011), Climatology of the nighttime equatorial thermospheric winds and temperatures over Brazil near solar minimum, *J. Geophys. Res.*, 116, A04322, doi:10.1029/2011JA016477.
- Oberheide, J., J. Forbes, X. Zhang, and S. Bruinsma (2011), Climatology of upward propagating diurnal and semidiurnal tides in the thermosphere, *J. Geophys. Res.*, 116, A11306, doi:10.1029/2011JA016784.
- Richards, P. (1991), An improved algorithm for determining neutral winds from the height of the F₂ peak electron density, *J. Geophys. Res.*, 96(A10), 17,839–17,846, doi:10.1029/91JA01467.
- Richmond, A. (1995), Ionospheric electrodynamics using magnetic apex coordinates, *J. Geomagn. Geoelec.*, 47(2), 191–212.
- Richmond, A., E. Ridley, and R. Roble (1992), A thermosphere/ionosphere general circulation model with coupled electrodynamics, *Geophys. Res. Lett.*, 19(6), 601–604, doi:10.1029/92GL00401.
- Ridley, A., Y. Deng, and G. Toth (2006), The global ionosphere—Thermosphere model, *J. Atmos. Sol. Terr. Phys.*, 68(8), 839–864, doi:10.1016/j.jastp.2006.01.008.
- Rishbeth, H. (1972), Thermospheric winds and F-region: Review, *J. Atmos. Terr. Phys.*, 34(1), 1–47, doi:10.1016/0021-9169(72)90003-7.
- Roble, R. (2000), On the feasibility of developing a global atmospheric model extending from the ground to the exosphere, in *Atmospheric Science Across the Stratopause*, edited by D. E. Siskind et al., pp. 53–67, AGU, Washington, D.C.
- Roble, R. G., R. Dickinson, E. Ridley, B. Emery, P. Hays, T. L. Killeen, and N. W. Spencer (1983), The high latitude circulation and temperature structure of the thermosphere near solstice, *Planet. Space Sci.*, 31(12), 1479–1499, doi:10.1016/0032-0633(83)90021-1.
- Rodgers, C. D. (2000), *Inverse Methods For Atmospheric Sounding: Theory and Practice*, vol. 2, World Sci., Singapore.
- Ruan, H., J. Lei, X. Dou, S.-R. Zhang, J. Noto, and S. Kapali (2013), Enhancements of nighttime neutral and ion temperatures in the F region over Millstone Hill, *J. Geophys. Res. Space Physics*, 118, 1768–1776, doi:10.1002/jgra.50202.
- Salah, J., and J. Holt (1974), Midlatitude thermospheric winds from incoherent scatter radar and theory, *Radio Sci.*, 9(2), 301–313, doi:10.1029/RS009i002p00301.
- Sassi, F., H.-L. Liu, J. Ma, and R. R. Garcia (2013), The lower thermosphere during the northern hemisphere winter of 2009: A modeling study using high-altitude data assimilation products in WACCM-X, *J. Geophys. Res. Atmos.*, 118, 8954–8968, doi:10.1002/jgrd.50632.
- Scherliess, L., and B. G. Fejer (1999), Radar and satellite global equatorial F region vertical drift model, *J. Geophys. Res.*, 104(A4), 6829–6842, doi:10.1029/1999JA000025.
- Sipler, D. P., B. B. Luokkala, and M. A. Biondi (1982), Fabry-Perot determinations of midlatitude F-region neutral winds and temperatures from 1975 to 1979, *Planet. Space Sci.*, 30(10), 1025–1032.
- Siskind, D., D. Drob, K. Dymond, and J. McCormack (2014), Simulations of the effects of vertical transport on the thermosphere and ionosphere using two coupled models, *J. Geophys. Res. Space Physics*, 119, 1172–1185, doi:10.1002/2013JA019116.
- Siskind, D. E., and D. P. Drob (2014), Use of NOGAPS-ALPHA as a bottom boundary for the NCAR/TIEGCM, in *Modeling the Ionosphere-Thermosphere System*, edited by J. Huba, R. Schunk, and G. Khazanov, pp. 171–180, John Wiley, Chichester, U.K., doi:10.1002/9781118704417.ch15.
- Siskind, D. E., D. P. Drob, J. T. Emmert, M. H. Stevens, P. E. Sheese, E. J. Llewellyn, M. E. Hervig, R. Niciejewski, and A. J. Kochenash (2012), Linkages between the cold summer mesopause and thermospheric zonal mean circulation, *Geophys. Res. Lett.*, 39, L01804, doi:10.1029/2011GL050196.
- Spencer, N., L. Wharton, H. Niemann, A. Hedin, G. Carrigan, and J. Maurer (1981), The dynamics explorer wind and temperature spectrometer, *Space Sci. Instrum.*, 5, 417–428.
- Swarztrauber, P. N. (1993), The vector harmonic transform method for solving partial differential equations in spherical geometry, *Mon. Weather Rev.*, 121(12), 3415–3437, doi:10.1175/1520-0493(1993)121<3415:TVHTMF>2.0.CO;2.
- Wang, W., A. Burns, M. Wilbertser, S. Solomon, and T. Killeen (2008), Altitude variations of the horizontal thermospheric winds during geomagnetic storms, *J. Geophys. Res.*, 113, A02301, doi:10.1029/2007JA012374.
- Yasyukevich, Y. V., E. Afraimovich, K. Palamartchouk, and P. Tatarinov (2010), Cross testing of ionosphere models IRI-2001 and IRI-2007, data from satellite altimeters (Topex/Poseidon and Jason-1) and global ionosphere maps, *Adv. Space Res.*, 46(8), 990–1007, doi:10.1016/j.asr.2010.06.010.